GEOPHYSICS, VOL. 78, NO. 2 (MARCH-APRIL 2013); P. WA41–WA54, 8 FIGS., 5 TABLES.
10.1190/GEO2012-0332.1

Wavefield decomposition based on acoustic reciprocity: Theory and applications to marine acquisition

Roald Gunnar van Borselen[1], Jacob Fokkema[2], and Peter van den Berg[2]

ABSTRACT

In marine seismic acquisition, the free surface generates seismic events in our recorded data that are often categorized as noise because these events do not contain independent information about the subsurface geology. Ghost events are considered as such noise because these events are generated when the energy generated by the seismic source, as well as any upgoing wavefield propagating upward from the subsurface, is reflected downward by the free surface. As a result, complex interference patterns between up- and downgoing wavefields are present in the recorded data, affecting the spectral bandwidth of the recorded data negatively. The interpretability of the data is then compromised, and hence it is desirable to remove the ghost events from the data. Rayleigh's reciprocity theorem is used to derive the relevant equations for wavefield decomposition for multisensor and single-sensor data, for depth-varying and depth-independent recordings from marine seismic experiments using a single-source or dual-source configuration. A comparison is made between the results obtained for a 2D synthetic example designed to highlight the strengths and weaknesses of the various acquisition configurations. It is demonstrated that, using the proposed wavefield decomposition method, multisensor data (measurements of pressure and particle velocity components, or multidepth pressure measurements) allow for optimal wavefield decomposition as independent measurements are used to eliminate the interference patterns caused by the free surface. Single-sensor data using constant-depth recordings are found to be incapable of producing satisfactory results in the presence of noise. Single-sensor data using a configuration with depth-varying measurements are able to deliver better results than when constant-depth recordings are used, but the results obtained are not of the same quality when multisensor data are used.

INTRODUCTION

In recent years, new acquisition systems have been introduced to marine seismic acquisition to increase the bandwidth and resolution of the recorded data. These methods all aim to remove the so-called ghost reflections that have been generated by the free surface. The free surface reflects the seismic energy back into the water layer such that any seismic event is recorded twice: first as an upgoing wavefield that has been reflected by the subsurface and secondly as a ghost, which is the downgoing field that has been reflected by the free surface. This receiver ghost has the opposite polarity from the upgoing wavefield, causing peaks and notches in the amplitude spectrum of the recorded data, due to the interference of the up- and downgoing wavefields. Similarly, the seismic energy omitted by the seismic sources consists of two constituents: one component propagates directly downward into the subsurface, and the second component, often referred to as the "source ghost," first propagates upward to the free surface before it is reflected off the free surface again to propagate as a downgoing wavefield. As a result of the source and receiver ghosts, the temporal resolution of the data is reduced.

In multisensor acquisition, this problem of receiver ghost events is overcome through the use of streamers where hydrophones and velocity sensors are collocated at the same depth. Because the velocity sensors are directional, the downgoing velocity wavefield, being phase reversed by reflection at the free surface is measured as having the same polarity to the upgoing velocity wavefield. As a result, the receiver ghost notches for the pressure and particle

Manuscript received by the Editor 16 August 2012; revised manuscript received 19 December 2012; published online 21 March 2013; corrected version published online 8 April 2013.
[1]PGS, Leiden, The Netherlands. E-mail: roald.van.borselen@pgs.com.
[2]Delft University of Technology, Delft, The Netherlands. E-mail: j.t.fokkema@tudelft.nl; p.m.vandenBerg@tudelft.nl.

velocity sensors are exactly interleaved in the frequency domain. When signals from the two sensors are properly combined, the ghost reflection cancels and the bandwidth of the recorded data is significantly increased (Pharez et al., 2008; Tenghamn and Dhelie, 2009).

Another approach is to record the pressure wavefield at two different constant depths (Moldoveanu et al., 2007). As the interference patterns of the events are different for the two independent recordings, the measured wavefields can be combined to eliminate the receiver ghosts from the recorded data.

A third approach to address the receiver ghosts is to measure the data using a single pressure sensor only, but to measure the data at variable depths (Soubaras and Dowle, 2010). Because the interference patterns are directly dependent on the depth where the measurements are taken, the ghost notches will have a more diverse character, which can reduce the impact of the notches in the seismic spectrum of the recorded data.

To address the source ghosts, an acquisition system can be designed such that two (or more) independent seismic experiments are conducted in which the depths of the seismic sources for the independent experiments are chosen such that the recorded data can be combined to eliminate the interference effects caused by the free surface (Egan et al., 2007; Parkes and Hegna, 2011).

A key component in the delivery of increased bandwidth and resolution is the ability to decompose the recorded into up- and downgoing constituents, thereby removing the source and receiver ghost events from the measured data. In this paper, the fundamentals of acoustic wavefield decomposition are revisited. We choose the reciprocity theorem as the central theme because it constitutes the fundaments of the seismic wave theory and it allows for a consistent and hierarchical description of seismic wavefield decomposition. We will derive and analyze the equations for wavefield decomposition for multisensor and single-sensor data, for depth-varying and depth-independent recordings from experiments using a single- or dual-source configuration.

We will concentrate on the seismic problem, in which the measurement is a sampled version of the acoustic wavefield. As such, the derivations are based on the acoustic wave equations and the constitutive parameters are the mass density and the compressibility.

First, we discuss the mathematical tools we use in the analysis of the acoustic wavefield, and we briefly discuss the partial differential equations that govern the dynamical state of matter on a macroscopic scale and hence the acoustic wave propagation in the medium. We will also state the expressions for the acoustic wavefield that is causally related to the action of sources of bounded extent in an unbounded homogeneous medium.

Next, we will introduce the concepts of acoustic states, defined in a time-invariant, bounded domain. They encompass the set of circumstances that completely describes the wave motion in the domain of consideration. We distinguish three constitutive members of the set: the material state, which relates to the parameter distribution; the source state, which corresponds to the source distribution; and the field state, which represents the induced wavefield quantities. Then, we will discuss the reciprocity theorem. This theorem relates two nonidentical acoustic states that can occur in the domain of interest. It directly relates the spatial divergence of the wavefield interaction quantity to the differences between the material and the source distributions of the two states. In the Laplace-transform domain, we present two forms of this theorem: the field reciprocity theorem and the power reciprocity theorem. Both forms of the reciprocity theorem are important for a consistent decomposition analysis.

We will formalize wavefield decomposition with the aid of the reciprocity theorems. We consider a homogeneous subdomain of infinite lateral extent, bounded vertically by two interfaces. The wavefield decomposition is realized in a horizontal plane of this region. With the aid of the field reciprocity theorem and the causal Green's function, we show that the downgoing wavefield is associated with an integral contribution of time-retarded surface-source distributions over the upper interface. Using the power reciprocity theorem and the anticausal Green's function, we obtain an integral expression for the upgoing wavefield in terms of time-advanced surface-source distributions over the upper interface. The fact that the down- and upgoing parts are related to the upper interface makes the decomposition feasible in surface seismics. The theoretical development presented in this paper finds its origin in Fokkema and van den Berg (1993).

MATHEMATICAL FRAMEWORK

The seismic quantities that describe the acoustic waves depend on position and on time. Their time dependence in the domain in which the seismic source is acting is impressed by the excitation mechanism of the source. The subsequent dependence on position and time is governed by propagation and scattering laws.

To register the position we use a Cartesian reference frame with three base vectors $\{\mathbf{i}_1, \mathbf{i}_2, \mathbf{i}_3\}$ that are mutually perpendicularly oriented and are of unit length each. The property that each base vector specifies geometrically a length and an orientation makes it a vectorial quantity, or a vector; notationally, vectors will be represented by bold-face symbols. Let $\{x_1, x_2, x_3\}$ denote the three numbers that are needed to specify the position of an observer, then the vectorial position of the observer $\mathbf{x}$ is the linear combination

$$\mathbf{x} = x_1\mathbf{i}_1 + x_2\mathbf{i}_2 + x_3\mathbf{i}_3. \tag{1}$$

The numbers $\{x_1, x_2, x_3\}$ are denoted as the orthogonal Cartesian coordinates of the point of observation.

To register the time, we consider an interval $\mathbb{T} = \{t \in \mathbb{R}; t > t_0\}$, where t_0 is the switching time of the acting sources.

The forward Laplace transformation from the space-time domain $(\mathbf{x}, t)$ to the Laplace domain $(\mathbf{x}, s)$ is defined as

$$\hat{u}(\mathbf{x}, s) = \int_{t\in\mathbb{T}} \exp(-st)\chi_{\mathbb{T}}(t)u(\mathbf{x}, t)\mathrm{d}t, \tag{2}$$

and the corresponding backward Laplace transformation is defined as

$$\chi_{\mathbb{T}}(t)u(\mathbf{x}, t) = \frac{1}{2\pi j}\int_{s=-j\infty}^{s=+j\infty} \exp(st)\hat{u}(\mathbf{x}, s)\mathrm{d}s, \tag{3}$$

where t is time, $j = \sqrt{-1}$ is the imaginary unit, and s is a Laplace frequency parameter. In the Laplace transformation given above in equations 2 and 3, the Laplace parameter s, the frequency parameter, is conventionally a purely imaginary number and is defined as

$$s = j\omega = j2\pi f, \tag{4}$$

where ω is the circular frequency and f is the real frequency. Finally, the characteristic function is given by

$$\chi_{\mathbb{T}} = \begin{cases} 1 & \text{for} \quad t \in \mathbb{T}, \\ 1/2 & \text{for} \quad t \in \partial\mathbb{T}, \\ 0 & \text{for} \quad t \in \mathbb{T}', \end{cases} \tag{5}$$

in which the three subdomains are given by $\mathbb{T} = \{t \in \mathbb{R}; t > t_0\}$, $\partial\mathbb{T} = \{t \in \mathbb{R}; t = t_0\}$, and $\mathbb{T}' = \{t \in \mathbb{R}; t < t_0\}$, respectively; $\partial\mathbb{T}$ is the boundary of $\mathbb{T}$; whereas $\mathbb{T}'$ is the complement of $\mathbb{T} \cup \partial\mathbb{T}$.

As will be discussed later, it may be beneficial to consider a "complex" Laplace frequency parameter s that is a complex variable with real and imaginary parts; i.e.,

$$s = j\omega + \varepsilon = j2\pi f + \varepsilon, \tag{6}$$

where ε is an additional real part of the complex Laplace frequency parameter s.

It is common in seismic problems to assign the x_3-coordinate to the vertical depth position. Then, x_1 and x_2 represent the horizontal positions. Let us consider the scalar wavefield quantity $u = u(\mathbf{x}, t)$ and let $\hat{u} = \hat{u}(\mathbf{x}, s)$ denote its time Laplace transform. The spatial Fourier transform pair $\{\mathbf{F}, \mathbf{F}^{-1}\}$ of function $\hat{u}$ is then defined as

$$\begin{aligned} \mathbf{F}\{\hat{u}(x_1, x_2, x_3, s)\} &= \bar{u}(js\alpha_1, js\alpha_2, x_3, s) \\ &= \int_{(x_1,x_2)\in R^3} \exp(js\alpha_1 x_1 \\ &\quad + js\alpha_2 x_2)\hat{u}(x_1, x_2, x_3)\mathrm{d}A, \end{aligned} \tag{7}$$

$$\begin{aligned} &\frac{1}{(2\pi)^2} \int_{(s\alpha_1,s\alpha_2)\in R^3} \exp(-js\alpha_1 x_1, -js\alpha_2 x_2)\bar{u}(js\alpha_1, js\alpha_2, x_3, s)\mathrm{d}A \\ &= \hat{u}(x_1, x_2, x_3, s) = \mathbf{F}^{-1}\{\bar{u}(js\alpha_1, js\alpha_2, x_3, s)\}, \end{aligned} \tag{8}$$

in which $\{\alpha_1, \alpha_2\}$ are the horizontal components of the angular-slowness vector $\boldsymbol{\alpha}$, defined in terms of its Cartesian components

$$\boldsymbol{\alpha} = \alpha_1 \mathbf{i}_1 + \alpha_2 \mathbf{i}_2 + \alpha_3 \mathbf{i}_3, \tag{9}$$

where $\boldsymbol{\alpha}$ may be complex but $\mathbf{s}\boldsymbol{\alpha}$ is always taken to be real.

The acoustic wave equations are representative for the action of mechanical forces and the influence of inertia during the acoustic wave motion as well as of the deformation that take place during this wave motion. The acoustic wave motion is a dynamical state of matter that is superimposed on a static equilibrium state. In this respect, we shall only retain the first-order terms to describe the acoustic wave motion.

The basic acoustic wave equations in their low-velocity approximation (Fokkema and van den Berg, 1993) are given by

$$\partial_k p + \rho\partial_t v_k = f_k, \tag{10}$$

$$\partial_k v_k + \kappa\partial_t p = q, \tag{11}$$

in which p is the acoustic pressure in (Pa), f_k is the volume source density of volume force (N/m^3), v_k represents the particle velocity (m/s), q volume source density of injection rate (s^{-1}), ∂_t denotes differentiation with respect to time, and ∂_k represents differentiation with respect to spatial coordinates x_k, $k = 1, 2, 3$. Note that the summation convention for repeated subscripts applies; in particular $\partial_k v_k = \partial_1 v_1 + \partial_2 v_2 + \partial_3 v_3$.

When the constitutive parameters change continuously with position, the acoustic pressure and the particle velocity are continuously differentiable functions of position and satisfy the differential equations. In practice, of course it often occurs that fluids with different material parameters are in contact along interfaces. To interrelate the acoustic wavefield quantities at either side of an interface ∂D, with normal vector v_k, the pressure p and the particle velocity in the direction perpendicular across this interface $v_k v_k$ are continuous.

In the Laplace-transform domain, the acoustic wave equations have the form

$$\partial_k \hat{p} + s\rho\hat{v}_k = \hat{f}_k, \tag{12}$$

$$\partial_k \hat{v}_k + s\kappa\hat{p} = \hat{q}, \tag{13}$$

and the boundary conditions are such that pressure $\hat{p}$ and the particle velocity in the direction perpendicular across interface S, $v_k\hat{v}_k$ are continuous across S.

Reciprocity theorems

Next, we discuss the reciprocity theorems. These theorems constitute the fundament of the seismic wave theory. In the reciprocity theorems, we consider a time-invariant, bounded, domain D in space in which two nonidentical acoustic states can occur. The two states will be distinguished by the superscripts A and B, respectively. Neither the source distributions of the acoustic wavefields in the two states nor the fluids present in the two states need to be the same. The boundary surface of D is denoted by ∂D, the normal vector v_k on ∂D is directed away from D. The complement of $D \cup \partial D$ in $\mathbb{R}^3$ is denoted by D' (see Figure 1). We characterize the acoustic properties of the fluids by the volume density of mass $\rho = \rho(\mathbf{x})$ and the compressibility $\kappa = \kappa(\mathbf{x})$.

We start with the basic acoustic wavefield equations in the s-domain, as discussed in equations 12 and 13. State A is characterized by the acoustic wavefield $\{\hat{p}^A, \hat{v}_k^A\}$ the constitutive parameters $\{\rho^A, \kappa^A\}$ and the source distributions $\{\hat{q}^A, \hat{f}_k^A\}$. Similarly, state B is characterized by the acoustic wavefield $\{\hat{p}^B, \hat{v}_k^B\}$ the constitutive parameters $\{\rho^B, \kappa^B\}$ and the source distributions $\{\hat{q}^B, \hat{f}_k^B\}$ (see Table 1). The acoustic wavefield equations pertaining to state A and state B are then

$$\partial_k \hat{p}^A + s\rho^A \hat{v}_k^A = \hat{f}_k^A, \tag{14}$$

$$\partial_k \hat{v}_k^A + s\kappa^A \hat{p}^A = \hat{q}^A, \tag{15}$$

and

$$\partial_k \hat{p}^B + s\rho^B \hat{v}_k^B = \hat{f}_k^B, \tag{16}$$

$$\partial_k \hat{v}_k^B + s\kappa^B \hat{p}^B = \hat{q}^B, \tag{17}$$

respectively. In the s-domain field reciprocity relation, the interaction quantity between the two states is

$$\partial_k(\hat{p}^A\hat{v}_k^B - \hat{p}^B\hat{v}_k^A) = \hat{v}_k^B\partial_k\hat{p}^A + \hat{p}^A\partial_k\hat{v}_k^B - \hat{v}_k^A\partial_k\hat{p}^B - \hat{p}^B\partial_k\hat{v}_k^A. \quad (18)$$

Using equations 14–17, and after integration, the global form of the field reciprocity theorem is arrived at as

$$\int_{x\in\partial D}(\hat{p}^A\hat{v}_k^B - \hat{p}^B\hat{v}_k^A)_k\mathrm{d}A = \int_{x\in D}[s(\rho^B-\rho^A)\hat{v}_k^A\hat{v}_k^B - s(\kappa^B-\kappa^A)\hat{p}^A\hat{p}^B]\mathrm{d}V + \int_{x\in D}(\hat{f}_k^A\hat{v}_k^B + \hat{q}^B\hat{p}^A - \hat{f}_k^B\hat{v}_k^A - \hat{q}^A\hat{p}^B)\mathrm{d}V. \quad (19)$$

In the s-domain power reciprocity theorem, we again consider two states A and B in a bounded domain. State A is again characterized by the acoustic wavefield $\{\hat{p}^A, \hat{v}_k^A\}$, the constitutive parameters $\{\rho^A, \kappa^A\}$, and the source distributions $\{\hat{q}^A, \hat{f}_k^A\}$. State B is now characterized by the anticausal acoustic wavefield $\{\hat{p}^B, \hat{v}_k^B\} = \{\hat{p}^B, \hat{v}_k^B\}(\mathbf{x}, -s)$, the constitutive parameters $\{\rho^B, \kappa^B\}$, and the source distributions $\{\hat{q}^B, \hat{f}_k^B\} = \{\hat{q}^B, \hat{f}_k^B\}(\mathbf{x}, -s)$, recognized as the anticausal counterpart (see Table 2). The acoustic wavefield equations pertaining to state A and state B are then

$$\partial_k\hat{p}^A + s\rho^A\hat{v}_k^A = \hat{f}_k^A, \quad (20)$$

$$\partial_k\hat{v}_k^A + s\kappa^A\hat{p}^A = \hat{q}^A, \quad (21)$$

and

$$\partial_k\hat{p}^B - s\rho^B\hat{v}_k^B = \hat{f}_k^B, \quad (22)$$

$$\partial_k\hat{v}_k^B - s\kappa^B\hat{p}^B = \hat{q}^B, \quad (23)$$

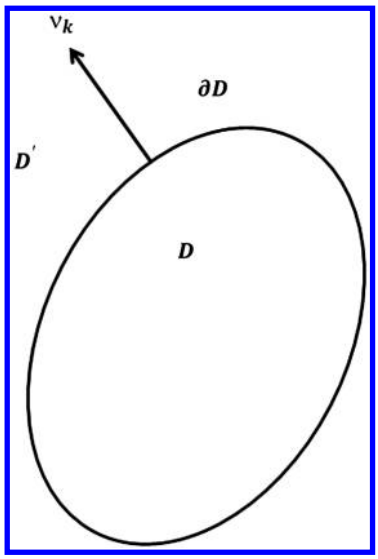

Figure 1. Configuration for the application of the reciprocity theorem.

respectively. In the s-domain power reciprocity relation, the interaction quantity between the two states is

$$\partial_k(\hat{p}^A\hat{v}_k^B + \hat{p}^B\hat{v}_k^A) = \hat{v}_k^B\partial_k\hat{p}^A + \hat{p}^A\partial_k\hat{v}_k^B + \hat{v}_k^A\partial_k\hat{p}^B + \hat{p}^B\partial_k\hat{v}_k^A. \quad (24)$$

Using equations 20–23, and after integration, the global form of the power reciprocity theorem is arrived at as

$$\int_{x\in\partial D}(\hat{p}^A\hat{v}_k^B + \hat{p}^B\hat{v}_k^A)_k\mathrm{d}A = \int_{x\in D}[s(\rho^B-\rho^A)\hat{v}_k^A\hat{v}_k^B + s(\kappa^B-\kappa^A)\hat{p}^A\hat{p}^B]\mathrm{d}V + \int_{x\in D}(\hat{f}_k^A\hat{v}_k^B + \hat{q}^B\hat{p}^A + \hat{f}_k^B\hat{v}_k^A + \hat{q}^A\hat{p}^B)\mathrm{d}V. \quad (25)$$

Wavefield decomposition

Next, it will be demonstrated that in a horizontal plane in a homogeneous subdomain, the acoustic wavefield may be written as a superposition of the down- and upgoing wave constituents. In the analysis, the s-domain field and power reciprocity theorem will be used.

We consider two interfaces ∂D_0 and ∂D_1. We assume that the medium in the domain D between these interfaces is homogeneous with constitutive parameters ρ and κ. We further assume that the interface ∂D_0 and ∂D_1 do not overlap; i.e., $x_{3,\min}^{(1)} > x_{3,\max}^{(0)}$, where $x_{3,\max}^{(0)}$ denotes the maximum value of x_3 on the interface ∂D_0, whereas $x_{3,\min}^{(1)}$ denotes the minimum value of x_3 on the interface

Table 1. States in the field reciprocity theorem.

	State A	State B
Field state	$\{\hat{p}^A, \hat{v}_k^A\}(\mathbf{x}, s)$	$\{\hat{p}^B, \hat{v}_k^B\}(\mathbf{x}, s)$
Material state	$\{\rho^A, k^A\}(\mathbf{x})$	$\{\rho^B, k^B\}(\mathbf{x})$
Source state	$\{\hat{q}^A, \hat{f}_k^A\}(\mathbf{x}, s)$	$\{\hat{q}^B, \hat{f}_k^B\}(\mathbf{x}, s)$
Domain D (see Figure 1)		

Table 2. States in the power reciprocity theorem.

	State A	State B
Field state	$\{\hat{p}^A, \hat{v}_k^A\}(\mathbf{x}, s)$	$\{\hat{p}^B, \hat{v}_k^B\}(\mathbf{x}, -s)$
Material state	$\{\rho^A, k^A\}(\mathbf{x})$	$\{\rho^B, k^B\}(\mathbf{x})$
Source state	$\{\hat{q}^A, \hat{f}_k^A\}(\mathbf{x}, s)$	$\{\hat{q}^B, \hat{f}_k^B\}(\mathbf{x}, -s)$
Domain D (see Figure 1)		

∂D_1. This means that there always exists a horizontal plane at x_3^R such that $x_{3,\max}^{(0)} < x_3^R < x_{3,\min}^{(1)}$ (see Figure 2).

We apply the s-domain field reciprocity theorem to the domain D inside the interfaces ∂D_0 and ∂D_1 (see Figure 2). The normal v_k to the interfaces is directed toward the domain D. State A is taken to be the actual wavefield that is generated by sources confined to a bounded domain in D'. The wavefield of state B is taken as the volume-injection Green's state, generated by a point source of volume injection (see Table 3).

If we now define the Green's states to be as

$$\{\hat{p}^q, \hat{v}_k^q\}(\mathbf{x}|\mathbf{x}^R, s) = \hat{q}^B(s)\{\hat{G}^q, -\hat{\Gamma}_k^q\}(\mathbf{x}^R|\mathbf{x}, s), \tag{26}$$

then substitution of states A and B into equation 19 leads to

$$\begin{aligned}\hat{p}(\mathbf{x}^R, s) = \int_{x\in(\partial D_0\cup\partial D_1)} &[\hat{G}^q(\mathbf{x}^R|\mathbf{x}, s)\hat{v}_k(\mathbf{x}, s) \\ &+ \hat{\Gamma}_k^q(\mathbf{x}^R|\mathbf{x}, s)\hat{p}(\mathbf{x}, s)]v_k \mathrm{d}A, \\ \text{when } \mathbf{x}^R \in D,&\end{aligned} \tag{27}$$

in which

$$\hat{G}^q(\mathbf{x}^R|\mathbf{x}, s) = s\rho\hat{G}(\mathbf{x}^R - \mathbf{x}, s), \tag{28}$$

$$\hat{\Gamma}_k^q(\mathbf{x}^R|\mathbf{x}, s) = -\partial_k^R\hat{G}(\mathbf{x}^R - \mathbf{x}, s), \tag{29}$$

and the Green's function in the s-domain is defined as

$$\hat{G}(\mathbf{x}, s) = \frac{\exp\left(-\frac{s}{c}|\mathbf{x}|\right)}{4\pi|\mathbf{x}|}, \quad \text{with } c = (\kappa\rho)^{-\frac{1}{2}}. \tag{30}$$

In the derivation of equation 27, it has been taken into account that contributions of the bounding surfaces at $(x_1^2 + x_2^2) \to \infty$ vanish, because the integrand of equation 27 is of the order $[(x_1^2 + x_2^2)^{-1}]$ as $(x_1^2 + x_2^2) \to \infty$. The latter asymptotic behavior follows directly from the Green's function representation of equation 30 and its far-field approximations (Fokkema and van den Berg, 1993, Chapter 4). It is remarked that the wavefield at $\mathbf{x}^R$ consists of contributions of surfaces sources located on interfaces ∂D_0 and ∂D_1.

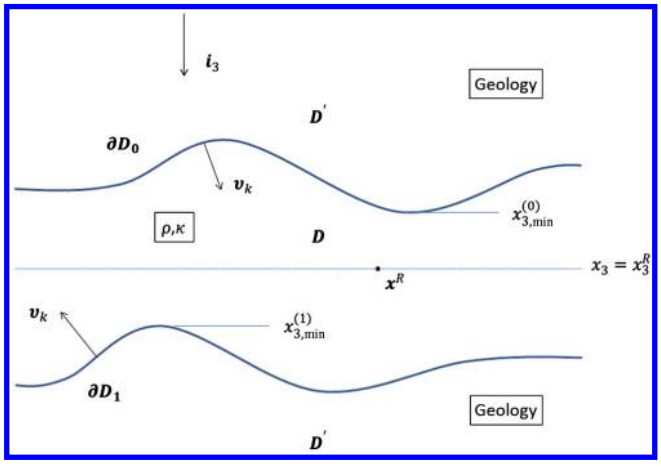

Figure 2. A homogeneous subdomain D bounded by the interfaces ∂D_0 and ∂D_1.

It is most convenient to carry the decomposition of the wavefield in the domain of the Fourier transform with respect to the horizontal coordinates. We therefore use the Fourier representation of the Green's function, given by

$$\bar{G}(js\alpha_1, js\alpha_2, x_3, s) = \frac{\exp(-s\Gamma|x_3|)}{2s\Gamma}, \tag{31}$$

where

$$\Gamma = \left(\frac{1}{c^2} + \alpha_1^2 + \alpha_2^2\right)^{\frac{1}{2}}, \qquad \mathrm{Re}(\Gamma) > 0. \tag{32}$$

Transforming equation 27 to the spatial Fourier domain, using the representations of equations 28, 29, and 31, noting that $|x_3^R - x_3| = x_3^R - x_3$ when $x \in \partial D_0$ and $|x_3^R - x_3| = x_3 - x_3^R$ when $x \in \partial D_1$, and interchanging the order of integrations, we arrive at the decomposition into the down- and upgoing wavefields:

$$\hat{p}(x_1, x_2, x_3^R, s) = \hat{p}^{\mathrm{down}}(x_1, x_2, x_3^R, s) + \hat{p}^{\mathrm{up}}(x_1, x_2, x_3^R, s), \tag{33}$$

where the spectral counterparts are given by

$$\bar{p}^{\mathrm{down}}(js\alpha_1, js\alpha_2, x_3^R, s) = \bar{P}^{\mathrm{down}}(js\alpha_1, js\alpha_2, s)\exp(-s\Gamma x_3^R), \tag{34}$$

$$\bar{p}^{\mathrm{up}}(js\alpha_1, js\alpha_2, x_3^R, s) = \bar{P}^{\mathrm{up}}(js\alpha_1, js\alpha_2, s)\exp(s\Gamma x_3^R). \tag{35}$$

The amplitude $\bar{P}^{\mathrm{down}}$ of the downgoing wavefield consists of contributions of surface sources at ∂D_0, whereas the amplitude $\bar{P}^{\mathrm{up}}$ of the upgoing wavefield consists of contributions of surface sources at ∂D_1. These amplitudes are expressed by

$$\begin{aligned}\bar{P}^{\mathrm{down}}&(js\alpha_1, js\alpha_2, s) \\ &= \frac{1}{2s\Gamma}\int_{x\in\partial D_0}[\hat{v}_k(\mathbf{x}, s)s\rho\,\exp(js\alpha_1 x_1 + js\alpha_2 x_2 + s\Gamma x_3) \\ &+ \hat{p}(\mathbf{x}, s)\partial_k\,\exp(js\alpha_1 x_1 + js\alpha_2 x_2 + s\Gamma x_3)]v_k \mathrm{d}A,\end{aligned} \tag{36}$$

and

Table 3. States in the field reciprocity theorem.

	State A (actual state)	State B (volume-injection Green's state)
Field state	$\{\hat{p}, \hat{v}_k\}(\mathbf{x}, s)$	$\{\hat{p}^q, \hat{v}_k^q\}(\mathbf{x}|\mathbf{x}^R, s)$
Material state	$\{\rho, k\}$	$\{\rho, k\}$
Source state	$\{0, 0\}$	$\{\hat{q}^B(\mathbf{s})\boldsymbol{\delta}(\mathbf{x} - \mathbf{x}^R), 0\}$
Domain D (see Figure 1)		

$$\bar{P}^{\mathrm{up}}(js\alpha_1, js\alpha_2, s) = \frac{1}{2s\Gamma}\int_{x\in\partial D_1}[\hat{v}_k(\mathbf{x},s)s\rho\,\exp(js\alpha_1 x_1 + js\alpha_2 x_2 - s\Gamma x_3) + \hat{p}(\mathbf{x},s)\partial_k\,\exp(js\alpha_1 x_1 + js\alpha_2 x_2 + s\Gamma x_3)]v_k\mathrm{d}A. \tag{37}$$

It is remarked that the particle velocity associated with the downgoing wavefield follows directly from equation 34 and wave equation (equation 13) in a source-free homogeneous medium. The vertical component of the particle velocity and the acoustic pressure of the downgoing wavefield are related to each other as

$$\rho\bar{v}_3^{\mathrm{down}}(js\alpha_1, js\alpha_2, x_3^R, s) - \Gamma\bar{p}^{\mathrm{down}}(js\alpha_1, js\alpha_2, s) = 0. \tag{38}$$

Similarly, the vertical component of the particle velocity and the acoustic pressure of the upgoing wavefield are related to each other as

$$\rho\bar{v}_3^{\mathrm{up}}(js\alpha_1, js\alpha_2, x_3^R, s) + \Gamma\bar{p}^{\mathrm{up}}(js\alpha_1, js\alpha_2, s) = 0. \tag{39}$$

The equations derived here show the decomposition in the down- and upgoing wavefields in a homogeneous subdomain of infinite extent in the horizontal directions. The downgoing wavefield $\hat{p}^{\mathrm{down}}(x_1, x_2, x_3^R, s)$ is obtained from the integral representation with surface contributions from ∂D_0 only. Similarly, the upgoing wavefield $\hat{p}^{\mathrm{up}}(x_1, x_2, x_3^R, s)$ is obtained from the integral representation with surface contributions from ∂D_1 only.

Multicomponent measurement decomposition from a single arbitrarily shaped recording interface

It may be that measurements are only made at a single surface contribution, either ∂D_0 or ∂D_1. Hence, it can be advantageous to derive equations that describe the upgoing wavefield from an integral representation with surface contributions from ∂D_0 only and the downgoing wavefield from the integral representation with surface contributions from ∂D_1 only.

To achieve this, we proceed as follows: We apply the s-domain power reciprocity theorem to the domain D inside the interfaces ∂D_0 and ∂D_1 (see Figure 2). State A is taken to be the actual wavefield that is generated by sources confined to a bounded domain in D'. The wavefield of state B is taken as the anticausal wavefield generated by a point source of volume injection (see Table 4).

Table 4. States in the power reciprocity theorem.

	State A (actual state)	State B (volume-injection Green's state)
Field state	$\{\hat{p}, \hat{v}_k\}(\mathbf{x}, s)$	$\{\hat{p}^q, \hat{v}_k^q\}(\mathbf{x}\|\mathbf{x}^R, -s)$
Material state	$\{\rho, k\}$	$\{\rho, k\}$
Source state	$\{0, 0\}$	$\{\hat{q}^B(-\mathbf{s})\boldsymbol{\delta}(\mathbf{x}-\mathbf{x}^R), 0\}$
Domain D (see Figure 1)		

Using the Green's states of equation 26, in which we replace s by $-s$, we arrive at

$$\hat{p}(\mathbf{x}^R, s) = \int_{x\in(\partial D_0\cup\partial D_1)}[-\hat{G}^q(\mathbf{x}^R|\mathbf{x}, -s)\hat{v}_k(\mathbf{x}, s) + \hat{\Gamma}_k^q(\mathbf{x}^R|\mathbf{x}, -s)\hat{p}(\mathbf{x}, s)]v_k\mathrm{d}A \quad \text{when } \mathbf{x}^R \in D, \tag{40}$$

in which for the anticausal Green's states for a homogeneous background, s is replaced by $-s$ in equations 28–30. In the derivation of equation 40, it has been taken into account again that contributions of the bounding surfaces at $(x_1^2 + x_2^2) \to \infty$ vanish, because the integrand of equation 40 is of the order $[(x_1^2 + x_2^2)^{-1}]$ as $(x_1^2 + x_2^2) \to \infty$.

We may also apply the reciprocity theorem to the domain D inside the interfaces ∂D_0 and ∂D_1, but now, state B is taken to be the anticausal counterpart of the actual wavefield, whereas state A is the causal wavefield generated by a point source of volume injection (see Table 5). We then arrive at

$$\hat{p}(\mathbf{x}^R, -s) = \int_{x\in(\partial D_0\cup\partial D_1)}[-\hat{G}^q(\mathbf{x}^R|\mathbf{x}, s)\hat{v}_k(\mathbf{x}-s) + \hat{\Gamma}_k^q(\mathbf{x}^R|\mathbf{x}, s)\hat{p}(\mathbf{x}-s)], v_k\mathrm{d}A, \quad \text{when } \mathbf{x}^R \in D. \tag{41}$$

Comparing equations 40 and 41, it is obvious that the causal actual wavefield can be obtained from equation 41 by replacing $-s$ by s.

To carry out the decomposition of the actual wavefield, we write the Green's function as a plane-wave representation, as

$$\hat{G}(\mathbf{x}, s) = \frac{1}{(2\pi^2)}\int_{(s\alpha_1, s\alpha_2)\in R^2}\frac{\exp(-js\alpha_1 x_1 - js\alpha_2 x_2 - s\Gamma|x_3|)}{2s\Gamma}\mathrm{d}A. \tag{42}$$

This representation is used in equations 28 and 29, and the results are substituted in the right side of equation 41. Changing the order of integrations, we then have

$$\hat{p}(\mathbf{x}^{\mathbf{R}}, -s) = \frac{1}{(2\pi^2)}\int_{(s\alpha_1, s\alpha_2)\in R^2}\frac{\exp(-js\alpha_1 x_1^R - js\alpha_2 x_2^R)}{2s\Gamma}\mathrm{d}A \times \int_{x\in(\partial D_0\cup\partial D_1)}[-\hat{v}_k(\mathbf{x}, -s)s\rho\,\exp(js\alpha_1 x_1 + js\alpha_2 x_2 - s\Gamma|\mathbf{x}^{\mathbf{R}} - \mathbf{x}|) + \hat{p}(\mathbf{x}, -s)\partial_k\,\exp(js\alpha_1 x_1 + js\alpha_2 x_2 - s\Gamma|\mathbf{x}^{\mathbf{R}} - \mathbf{x}|)]v_k\mathrm{d}A. \tag{43}$$

Reverting back to the causal wavefield by replacing $-s$ by s and noting that $|x_3^R - x_3| = x_3^R - x_3$ when $x \in \partial D_0$ and $|x_3^R - x_3| = x_3 - x_3^R$ when $x \in \partial D_1$, we arrive at the decomposition into the down- and upgoing wavefields:

$$\hat{p}(x_1, x_2, x_3^R, s) = \hat{p}^{\text{up}}(x_1, x_2, x_3^R, s) + \hat{p}^{\text{down}}(x_1, x_2, x_3^R, s), \tag{44}$$

where the spectral counterparts are given by

$$\bar{p}^{\text{up}}(js\alpha_1, js\alpha_2, x_3^R, s) = \bar{P}^{\text{up}}(js\alpha_1, js\alpha_2, s) exp(s\Gamma x_3^R), \tag{45}$$

$$\bar{p}^{\text{down}}(js\alpha_1, js\alpha_2, x_3^R, s) = \bar{P}^{\text{down}}(js\alpha_1, js\alpha_2, s) \exp(-s\Gamma x_3^R). \tag{46}$$

The amplitude $\bar{P}^{\text{up}}$ of the upgoing wavefield now consists of contributions of surface sources at ∂D_0, whereas the amplitude $\bar{P}^{\text{down}}$ of the downgoing wavefield consists of contributions of surface sources at ∂D_1. These amplitudes are expressed by

$$\begin{aligned}\bar{P}^{\text{up}}(js\alpha_1, js\alpha_2, s) &= \frac{-1}{2s\Gamma} \int_{x \in \partial D_0} [\hat{v}_k(\mathbf{x}, s) s\rho \exp(js\alpha_1 x_1 + js\alpha_2 x_2 - s\Gamma x_3) \\ &+ \hat{p}(\mathbf{x}, s) \partial_k \exp(js\alpha_1 x_1 + js\alpha_2 x_2 - s\Gamma x_3)] v_k \mathrm{d}A,\end{aligned} \tag{47}$$

$$\begin{aligned}\bar{P}^{\text{down}}(js\alpha_1, js\alpha_2, s) &= \frac{-1}{2s\Gamma} \int_{x \in \partial D_1} [\hat{v}_k(\mathbf{x}, s) s\rho \exp(js\alpha_1 x_1 + js\alpha_2 x_2 - s\Gamma x_3) \\ &+ \hat{p}(\mathbf{x}, s) \partial_k \exp(js\alpha_1 x_1 + js\alpha_2 x_2 - s\Gamma x_3)] v_k \mathrm{d}A.\end{aligned} \tag{48}$$

It is remarked that the particle velocity associated with the downgoing wavefield follows directly from equation 46 and wave equation (equation 13) in a source-free homogeneous medium. The vertical component of the particle velocity and the acoustic pressure of the downgoing wavefield are related to each other as

$$\rho \bar{v}_3^{\text{up}}(js\alpha_1, js\alpha_2, x_3^R, s) + \Gamma \bar{p}^{\text{up}}(js\alpha_1, js\alpha_2, x_3^R, s) = 0. \tag{49}$$

Similarly, the vertical component of the particle velocity and the acoustic pressure of the upgoing wavefield are related to each other as

$$\rho \bar{v}_3^{\text{down}}(js\alpha_1, js\alpha_2, x_3^R, s) - \Gamma \bar{p}^{\text{down}}(js\alpha_1, js\alpha_2, x_3^R, s) = 0. \tag{50}$$

The equations derived in this subsection show the decomposition in the down- and upgoing wavefields in a homogeneous subdomain of infinite extent in the horizontal directions. The upgoing wavefield $\hat{p}^{\text{up}}(x_1, x_2, x_3^R, s)$ is obtained from the integral representation with surface contributions from ∂D_0 only. Similarly, the downgoing wavefield $\hat{p}^{\text{down}}(x_1, x_2, x_3^R, s)$ is obtained from the integral representation with surface contributions from ∂D_1 only.

Equations 45–48, together with equations 34–37 derived from the field reciprocity allow for the computation of up- and downgoing wavefield constituents from a single measurement plane ∂D_0 or ∂D_1.

Multicomponent measurement decomposition from a single and plane recording interface

In the case that measurements are taken along ∂D_1 being a plane interface at $x_3 = x_3^{(1)}$, the expressions for the amplitudes in equations 37 and 48 reduce to

$$\begin{aligned}\bar{p}^{\text{up}}(js\alpha_1, js\alpha_2, x_3^R, s) &= \frac{\exp[s\Gamma(x_3^R - x_3^{(1)})]}{-2\Gamma} [\rho \bar{v}_3(js\alpha_1, js\alpha_2, x_3^{(1)}, s) \\ &- \Gamma \bar{p}(js\alpha_1, js\alpha_2, x_3^{(1)}, s)],\end{aligned} \tag{51}$$

$$\begin{aligned}\bar{p}^{\text{down}}(js\alpha_1, js\alpha_2, x_3^R, s) &= \frac{\exp[-s\Gamma(x_3^R - x_3^{(1)})]}{2\Gamma} [\rho \bar{v}_3(js\alpha_1, js\alpha_2, x_3^{(1)}, s) \\ &+ \Gamma \bar{p}(js\alpha_1, js\alpha_2, x_3^{(1)}, s)],\end{aligned} \tag{52}$$

after which the up- and downgoing constituents of the vertical component of the particle velocity can again be obtained from

$$\rho \bar{v}_3^{\text{up}}(js\alpha_1, js\alpha_2, x_3^R, s) + \Gamma \bar{p}^{\text{up}}(js\alpha_1, js\alpha_2, x_3^R, s) = 0, \tag{53}$$

$$\rho \bar{v}_3^{\text{down}}(js\alpha_1, js\alpha_2, x_3^R, s) - \Gamma \bar{p}^{\text{down}}(js\alpha_1, js\alpha_2, x_3^R, s) = 0. \tag{54}$$

It is remarked that no assumptions have been made so far about the free surface, not about its shape nor about its reflectivity. Provided that measurements of the pressure and vertical component of the particle velocity are available, a complete decomposition into up- and downgoing wavefield constituents is possible.

Single-measurement wavefield decomposition from a single and plane recording interface

In some instances, pressure and particle velocity measurements may not be available. In such cases, typically the pressure wavefield is measured only. We will now proceed to derive some equations for wavefield decomposition depending on pressure measurements only. It is remarked that a similar approach could be taken when only particle velocity measurements are available.

Table 5. States in the power reciprocity theorem.

	State A (volume-injection Green's state)	State B (actual state)
Field state	$\{\hat{p}^q, \hat{v}_k^q\}(\mathbf{x}\|\mathbf{x}^R, s)$	$\{\hat{p}, \hat{v}_k\}(\mathbf{x}, -s)$
Material state	$\{\rho, k\}$	$\{\rho, k\}$
Source state	$\{\hat{q}^B(\mathbf{s})\boldsymbol{\delta}(\mathbf{x} - \mathbf{x}^R), 0\}$	$\{0, 0\}$
Domain D (see Figure 1)		

When only pressure measurements are available, an additional constraint needs to be used to accomplish the decomposition. The additional constraint is used to construct the missing particle velocity measurements. We will assume that the total acoustic pressure vanishes at the free surface $x_3 = 0$. The aim is to determine the up- and downgoing constituents of the wavefield. In Fokkema and van den Berg (1993), this problem is considered as a wavefield decomposition problem (with the complication of the presence of a source in the homogeneous domain D), and solved using the field and power reciprocity theorem of the previous chapter. Here, we will take a simplified approach.

The total wavefield in a point $x \in D$, generated by a monopole source of the volume-injection type located at $\mathbf{x}^S$, is denoted as $\{\hat{p}, \hat{v}_k\}(\mathbf{x}|\mathbf{x}^S)$, and at the plane surface $x_3 = 0$ we have the boundary condition

$$\lim_{x_3 \downarrow 0} \hat{p}(\mathbf{x}|\mathbf{x}^s) = 0. \tag{55}$$

We first decompose the total pressure wavefield in the half-space $0 < x_3 < \infty$ into an incident wavefield and a scattered wavefield

$$\hat{p}(\mathbf{x}|\mathbf{x}^S) = \hat{p}^{\text{inc},H}(\mathbf{x}|\mathbf{x}^S) + \hat{p}^{\text{sct}}(\mathbf{x}|\mathbf{x}^S), \tag{56}$$

where the incident field is the wavefield that would be present in the half-space, if the domain D_g showed no contrast with the domain D (see Figure 3).

At a location x, we may write

$$\hat{p}^{\text{inc},H}(\mathbf{x}|\mathbf{x}^S) = s\rho\hat{q}^S\hat{G}^H(\mathbf{x}|\mathbf{x}^S), \tag{57}$$

where

$$\hat{G}^H(x|x^s, s) = \frac{\exp(-\frac{s}{c}|\mathbf{x} - \mathbf{x}^{\mathbf{s}}|)}{4\pi|\mathbf{x} - \mathbf{x}^{\mathbf{s}}|} - \frac{\exp(-\frac{s}{c}|\mathbf{x} - \mathbf{x}^{\mathbf{s}'}|)}{4\pi|\mathbf{x} - \mathbf{x}^{\mathbf{s}'}|}, \quad \text{with } c = (\kappa\rho)^{-\frac{1}{2}}, \tag{58}$$

and $x^{\mathbf{s}'} = (x_1^S, x_2^S, -x_3^S)$ denotes the image point of x^S with respect to the reflecting free surface at $x_3 = 0$. It can be observed that $\hat{p}^{\text{inc},H}$ vanishes at $x_3 = 0$ and that, therefore,

$$\lim_{x_3 \downarrow 0} \hat{p}^{\text{sct}}(\mathbf{x}|\mathbf{x}^s) = 0. \tag{59}$$

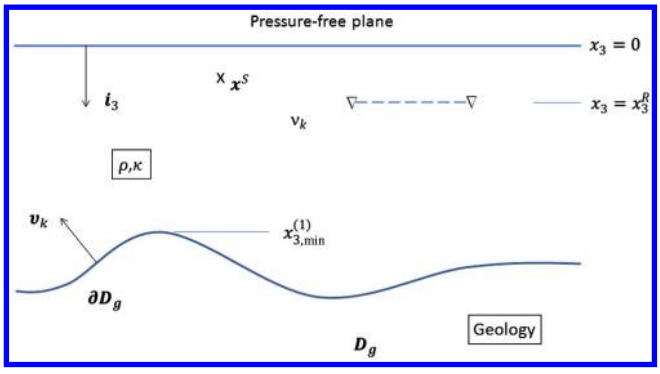

Figure 3. A homogeneous subdomain D bounded by the plane surface $x_3 = 0$ and the interface ∂D_g.

The scattered wavefield, defined as the difference between the total wavefield and incident wavefield, can be written as a sum of up- and downgoing wavefield constituents; i.e.,

$$\hat{p}^{\text{sct}}(x_1, x_2, x_3^R, s) = \hat{p}^{\text{down}}(x_1, x_2, x_3^R, s) + \hat{p}^{\text{up}}(x_1, x_2, x_3^R, s). \tag{60}$$

When only the scattered waves are considered, the domain D over which we considered the wavefield decomposition earlier will not contain sources. Hence, we can use the equations derived for wavefield decomposition to obtain equations for the up- and downgoing wavefield using pressure data only. Substitution of equation 59 into equations 34 and 36, where the boundary ∂D_0 of domain D is the free surface, leads to

$$\bar{p}^{\text{down}}(js\alpha_1, js\alpha_2, x_3, s) = \frac{\exp(-s\Gamma x_3)}{2\Gamma}\rho\bar{v}_3^{\text{sct}}(js\alpha_1, js\alpha_1, 0|\mathbf{x}^S, s). \tag{61}$$

Similarly, substitution of equation 59 into equations 45 and 47 leads to

$$\bar{p}^{\text{up}}(jx_1, js\alpha_2, x_3, s) = \frac{\exp(s\Gamma x_3)}{-2\Gamma}\rho\bar{v}_3^{\text{sct}}(js\alpha_1, js\alpha_1, 0|\mathbf{x}^S, s). \tag{62}$$

Summation of the two results leads to an expression for the unknown scattered vertical component of the particle velocity wavefield in terms of the measured scattered wavefield

$$v_3^{\text{sct}}(js\alpha_1, js\alpha_2, 0|\mathbf{x}^S, s) = \frac{-\Gamma}{\rho\,\sinh(s\Gamma x_3)}\bar{p}^{\text{sct}}(js\alpha_1, js\alpha_2, x_3|\mathbf{x}^S, s). \tag{63}$$

Combination of equations 62 and 63 then leads to an expression in the spatial Fourier domain for the upgoing pressure wavefield in terms of the measured scattered wavefield

$$\bar{p}^{\text{up}}(js\alpha_1, js\alpha_2, x_3|\mathbf{x}^S, s) = \frac{\exp(s\Gamma x_3)}{2\,\sinh x(s\Gamma x_3^R)}\bar{p}^{\text{sct}}(js\alpha_1, js\alpha_2, x_3^R|\mathbf{x}^S, s). \tag{64}$$

It is noted that this equation does not rely on any measurements of the particle velocity, which is due to the additional assumptions made related to the shape of the sea surface and its reflectivity. Although equation 64 suggests that the scattered wavefield can be decomposed into up- and downgoing wavefields in a straightforward way, it is remarked that a straightforward application leads to numerical instabilities when the denominator on the right side approaches zero. For a constant receiver depth x_3^R, this occurs for distinct combinations of imaginary Laplace frequency parameters and angular-slownesses α_1 and α_2, which are related to the angular frequency $\omega = 2\pi f$, where f is the frequency and the real slowness vector $\mathbf{p}$ by

$$s = j\omega, \tag{65}$$

$$\mathbf{p} = p_1\mathbf{i}_1 + p_2\mathbf{i}_2 + p_3\mathbf{i}_3 = j\alpha. \tag{66}$$

The numerical instabilities for certain frequency-slowness combinations, also known as notches, may be circumvented through the use of complex Laplace parameters (see equation 6), but it must be noted that the result will still be compromised by the fact that for those distinct $\{\omega, p_1, p_2\}$ combinations, the scattered pressure wavefield contains no relevant data.

Dual-pressure measurement decomposition from two plane recording interfaces

One way to circumvent the numerical instabilities in wavefield decomposition is to complement the pressure measurement with another pressure measurement at a different receiver depth. When two independent pressure measurements are available at the receiver depth $x_3^{R(1)}$ and $x_3^{R(2)}$, respectively, the application of equation 64 to both measurements, after least-squares summation, leads to

$$\begin{aligned}\bar{p}^{\text{up}}(js\alpha_1, js\alpha_2, x_3|\mathbf{x}^S, s) = \frac{\exp(s\Gamma x_3)}{2} \\ \cdot \left[\frac{\sinh(s\Gamma x_3^{R(1)})\hat{p}^{\text{sct}(1)}(js\alpha_1, js\alpha_2, x_3^{R(1)}|\mathbf{x}^S, s)}{|\sinh(s\Gamma x_3^{R(1)})|^2 + |\sinh(s\Gamma x_3^{R(2)})|^2}\right. \\ \left. + \frac{\sinh(s\Gamma x_3^{R(2)})\hat{p}^{\text{sct}(2)}(js\alpha_1, js\alpha_2, x_3^{R(2)}|\mathbf{x}^S, s)}{|\sinh(s\Gamma x_3^{R(1)})|^2 + |\sinh(s\Gamma x_3^{R(2)})|^2}\right].\end{aligned} \tag{67}$$

It is noted that receiver depths $x_3^{R(1)}$ and $x_3^{R(2)}$ can always be chosen such that the denominator of equation 67 will never approach zero. Obviously, in the derivation of equation 67, the same assumptions about the free surface were used as for the single pressure measurement case.

Single-measurement decomposition from a single depth-varying recording interface

Another way to circumvent the numerical instabilities in the decomposition of the measured scattered pressure wavefield is to take measurements of the scattered pressure wavefield at a variable depth, where the depth of the receiver depends on the offset between the source and the receivers. In such a case, the notches may pose less of a problem because the measured scattered pressure wavefield $\bar{p}^{\text{sct}}$ in the transformed domain will no longer be zero because of the diversity of receiver depths used. In other words, the notches in the transformed domain will be more diverse in their character.

When the receivers are located at arbitrary depths, the scattered wavefield in the spectral domain cannot be determined explicitly. Therefore, wavefield decomposition must be considered as a solution of an integral equation that, after discretization, can be obtained as the solution of a system of equations. For arbitrary $x^R = (x_1^R, x_2^R, x_3^R)$, the depth of the receivers are a single-valued function of the horizontal receiver coordinates; specifically, it is written as $x_3^R = x_3^R(x_1^R, x_2^R)$.

Transforming equation 64 back to the spatial domain, we arrive at

$$\begin{aligned}\hat{p}^{\text{up}}(x_1, x_2, x_3|\mathbf{x}^S, s) \\ = \mathbf{F}^{-1}\left\{\frac{\exp(s\Gamma x_3)}{2\sinh x(s\Gamma x_3^R)}\mathbf{F}\{p^{\text{sct}}(x_1, x_2, x_3^R|\mathbf{x}^S, s)\}\right\},\end{aligned} \tag{68}$$

in which $\{\mathbf{F}, \mathbf{F}^{-1}\}$ is the spatial Fourier transform pair defined by equations 6 and 7. Rewriting this explicitly to arrive at an integral equation for the scattered wavefield, we obtain

$$\begin{aligned}\int_{(s\alpha_1, s\alpha_2)\in R^2} K(x_1, x_2|js\alpha_1, js\alpha_2)\bar{p}^{\text{up}}(js\alpha_1, js\alpha_2, x_3|\mathbf{x}^S, s)\text{d}A \\ = \hat{p}^{\text{sct}}(x_1, x_2, x_3|\mathbf{x}^S, s),\end{aligned} \tag{69}$$

where the kernel K is defined by

$$\begin{aligned}K(x_1, x_2|js\alpha_1, js\alpha_2) = \exp(-js\alpha_1 x_1, -js\alpha_2 x_2) \\ \cdot \frac{2\sinh(s\Gamma x_3^R(x_1^R, x_2^R))}{\exp(s\Gamma x_3)}.\end{aligned} \tag{70}$$

This integral equation is ill-posed, because the kernel has a zero at the notches. However, because measurements are taken at a variable depth, the notches in the spectral domain are assumed to be less profound. In addition, a preconditioned conjugate gradient iterative scheme may overcome numerical instabilities (van Borselen et al., 2008, 2011).

Source wavefield decomposition

In all the derivations up to this point, the spatial Fourier transformations have been carried out with respect to the horizontal receiver coordinates of the scattered wavefield. However, for the scattered wavefield, the source and receiver coordinates can be interchanged due to physical reciprocity (Fokkema and van den Berg, 1993). As a result, for a fixed receiver position, carrying out the spatial Fourier transformations with respect to the horizontal source coordinates of the scattered field leads to decomposition into up- and downgoing source wavefield constituents. When the source and receiver decomposition are combined, an expression for the source- and receiver decomposed wavefield is obtained through

$$\begin{aligned}\hat{p}^{\text{deghost}}(\mathbf{x}^R|x_1, x_2, x_3, s) = \mathbf{F}^{-1}\left\{\frac{\exp(s\Gamma x_3)}{2\sinh x(s\Gamma x_3^S)}\right. \\ \left. \cdot \mathbf{F}\{p^{\boldsymbol{up}}(\mathbf{x}^R|x_1, x_2, x_3^S, s)\}\right\},\end{aligned} \tag{71}$$

in which $\{\mathbf{F}, \mathbf{F}^{-1}\}$ is the spatial Fourier transform pair defined by equations 7 and 8, now acting on the horizontal source coordinates. In the derivation of equation 71, the same assumptions with regards to the shape of the sea surface and its reflectivity are used as in the derivation of equation 64.

Wavefield decomposition: Numerical examples

In this section, we will demonstrate the different wavefield decomposition methods derived in the previous section using a single 2D configuration. The numerical data example is chosen to be simplistic to allow for an optimal analysis and comparison of the performance of the various methods.

We will first consider the case in which measurements are made using a recording streamer where the receiver depth is dependent on the distance between source and receiver. We will consider a single shot gather, with a point source located at a 5-m depth, and receivers

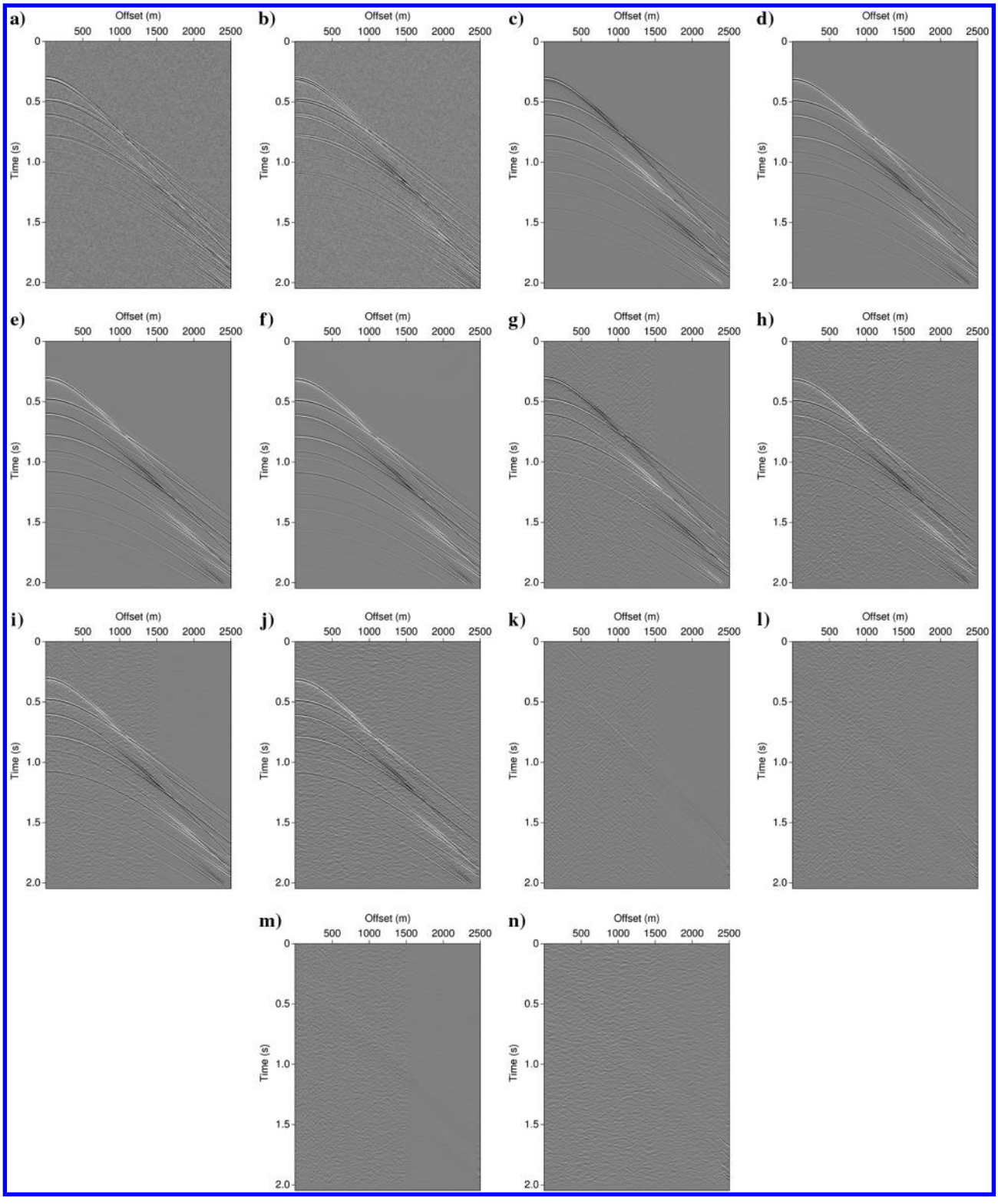

Figure 4. The modeled scattered pressure wavefield shot gather measured at variable depth (a), the modeled vertical component of the particle velocity measured at variable depth (b), the modeled upgoing pressure wavefield at reference depth 7.5 m (c), the modeled downgoing pressure wavefield at reference depth 7.5 m (d), the modeled upgoing vertical component of the particle velocity at reference depth 7.5 m (e), the modeled downgoing vertical component of the particle velocity at reference depth 7.5 m (f), the computed upgoing pressure wavefield at reference depth 7.5 m (g), the computed downgoing pressure wavefield at reference depth 7.5 m (h), the computed upgoing vertical component of the particle velocity at reference depth 7.5 m (i), the computed downgoing vertical component of the particle velocity at reference depth 7.5 m (j), and their respective differences (k)-(n).

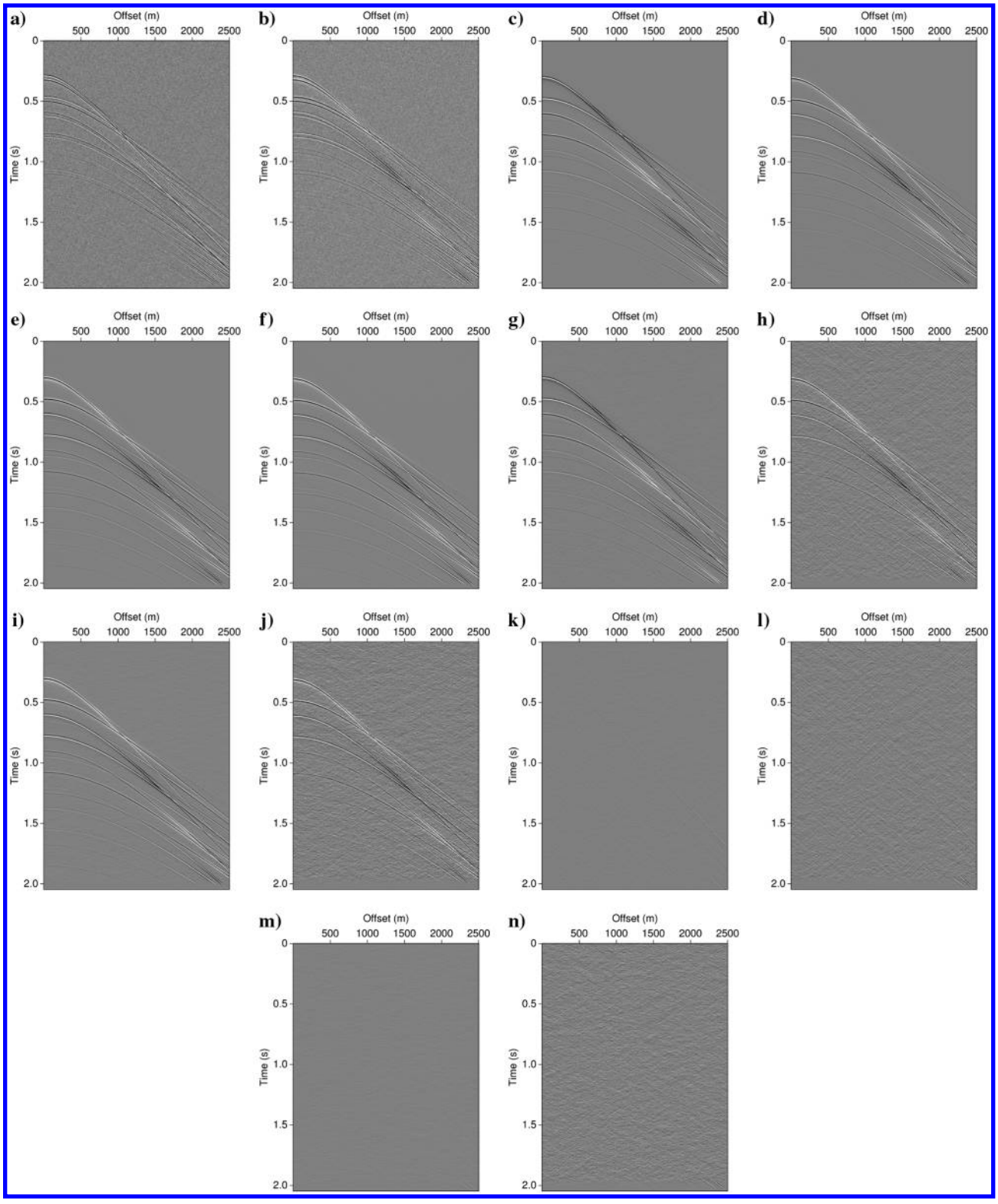

Figure 5. The modeled scattered pressure wavefield shot gather measured at a constant depth of 25 m (a), the modeled vertical component of the particle velocity measured at a constant depth of 25 m (b), the modeled (noise-free) upgoing pressure wavefield at a reference depth of 7.5 m (c), the modeled (noise-free) downgoing pressure wavefield at reference depth 7.5 m (d), the modeled (noise-free) upgoing vertical component of the particle velocity at reference depth 7.5 m (e), the modeled (noise-free) downgoing vertical component of the particle velocity at reference depth 7.5 m (f), the computed upgoing pressure wavefield at reference depth 7.5 m (g), the computed downgoing pressure wavefield at reference depth 7.5 m (h), the computed upgoing vertical component of the particle velocity at reference depth 7.5 m (i), the computed downgoing vertical component of the particle velocity at reference depth 7.5 m (j), and their respective differences (k)-(n).

are located behind the source with a receiver distance of 5 m, where the first receiver is at a 10-m depth, where the receiver depth is linearly increasing with offset (distance between the source and receiver) up to a 40-m depth at an offset of 1500 m and constant from 1500 up to 2500 m at a 40-m depth. The temporal sampling is 2 ms, and the recording length is 4000 s. The model consists of three layers: the first layer extends from the free surface to a depth of 225 m, the second layer extends to 225 to 400 m, and the third layer extends from 400 m to an infinite depth. The mass density of the fluid in the first layer is 1000 kg/m^3, and the compressibility is 2.96×10^{-10} Pa^{-1}, and the acoustic wave speed amounts to 1500 m/s. The mass density of the fluid in the second layer is 1500 kg/m^3, and the compressibility is 1.67×10^{-10} Pa^{-1}, whereas the acoustic wave speed amounts to 2000 m/s. The mass density of the fluid in the third layer is 1800 kg/m^3, and the compressibility is 8.89×10^{-11} Pa^{-1}, whereas the acoustic wave speed amounts to 2500 m/s. To make the analysis more realistic, Gaussian noise has been added to all modeled data, with a signal-to-noise ratio of 20. Figure 4a shows the modeled input shot gather with the scattered pressure wavefield, and Figure 4b shows the modeled normal component of the particle velocity field. Figure 4c–4f shows the modeled (noise-free) up- and downgoing pressure and vertical component of the particle velocity wavefield at a reference receiver depth of 7.5 m. Figure 4g–4j shows the results after using equations 37 and 48–50 for the up- and downgoing wavefield from measurements on ∂D_1 derived in the previous section. Note that the decomposition results contain less noise, from which can be deducted that the decomposition operators appear to reduce the noise content of the data. Figure 4k–4n shows the difference between the computed results and the reference results. Note the good agreement of the results and the minimal differences.

In the next example, we will consider the same 2D example, but now measurements are made using a recording streamer in which the receiver depth is independent on the distance between the source and receiver, located at a constant value of 25 m.

Figure 5a and 5b shows the modeled input shot gather for the scattered pressure and the vertical component of the particle velocity wavefield. Figure 5c–5f shows the modeled up- and downgoing pressure and vertical component of the particle velocity wavefield at a reference receiver depth of 7.5 m. Figure 5g–5j shows the results after using equations 51–54. Note again the reduced noise present in the data after decomposition Figure 5k–5n shows the difference between the computed results and the reference results. Note again the good agreement.

In the next example, we will consider the same pressure-measurement experiment, but now we use two recording streamers, located at two different but constant depths, 10 and 16 m, respectively. Figure 6a and 6b shows the modeled input pressure wavefield shot gathers, with the Gaussian noise added. Figure 6c shows the modeled upgoing pressure wavefield at a reference receiver depth of 7.5 m. Figure 6d shows the results after using equation 67, and Figure 6e shows the difference the computed results and the reference results. Note that the constant-depth two-streamer configuration appears to be able to cope with the spectral notches very well because no singularities in the denominator of equation 67 occur. We note again the reduced noise present in the data after decomposition.

In the next example, we will consider a pressure-measurement-only experiment, using a recording streamer in which the receiver

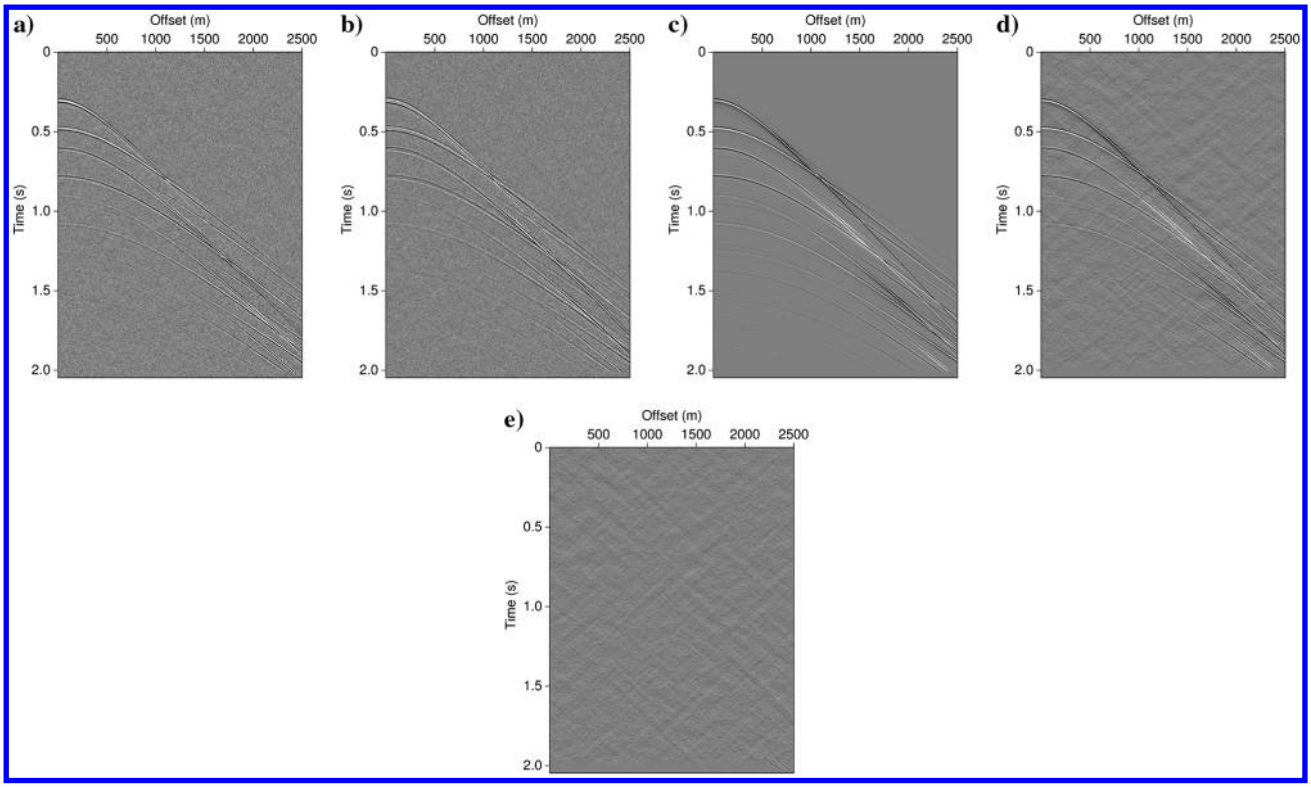

Figure 6. The modeled input scattered pressure wavefield shot gather measured at 10 m depth (a), the modeled input scattered pressure wavefield shot gather measured at 16 m depth (b), the modeled (noise-free) upgoing pressure wavefield at reference depth 7.5 m (c), the result of the decomposition using the dual scattered pressure data (d), and the difference (e).

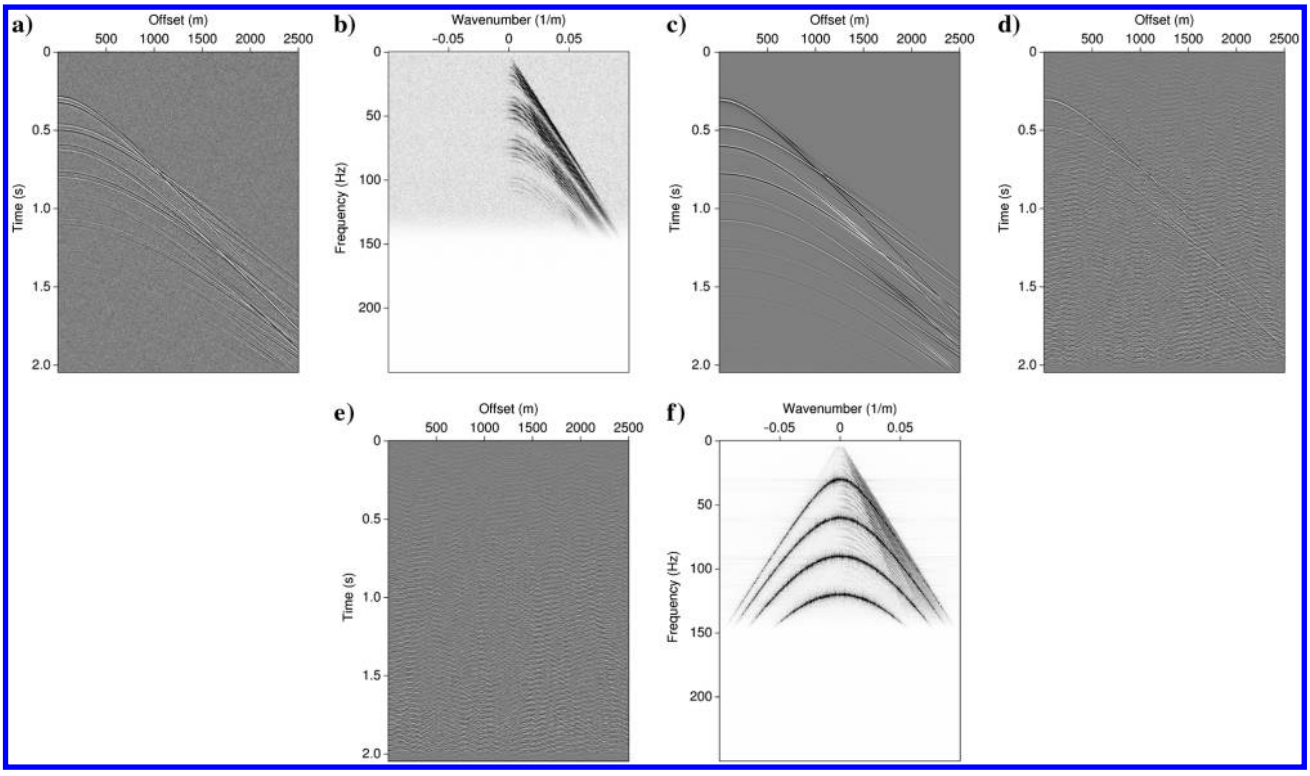

Figure 7. The modeled input scattered pressure wavefield shot gather for constant-depth measurements (a), the f-k spectrum of the shot record (b), the modeled upgoing pressure wavefield at reference depth 7.5 m (c), the result of the decomposition using the scattered pressure data only (d), the difference (e), and the f-k spectrum of the result obtained (f).

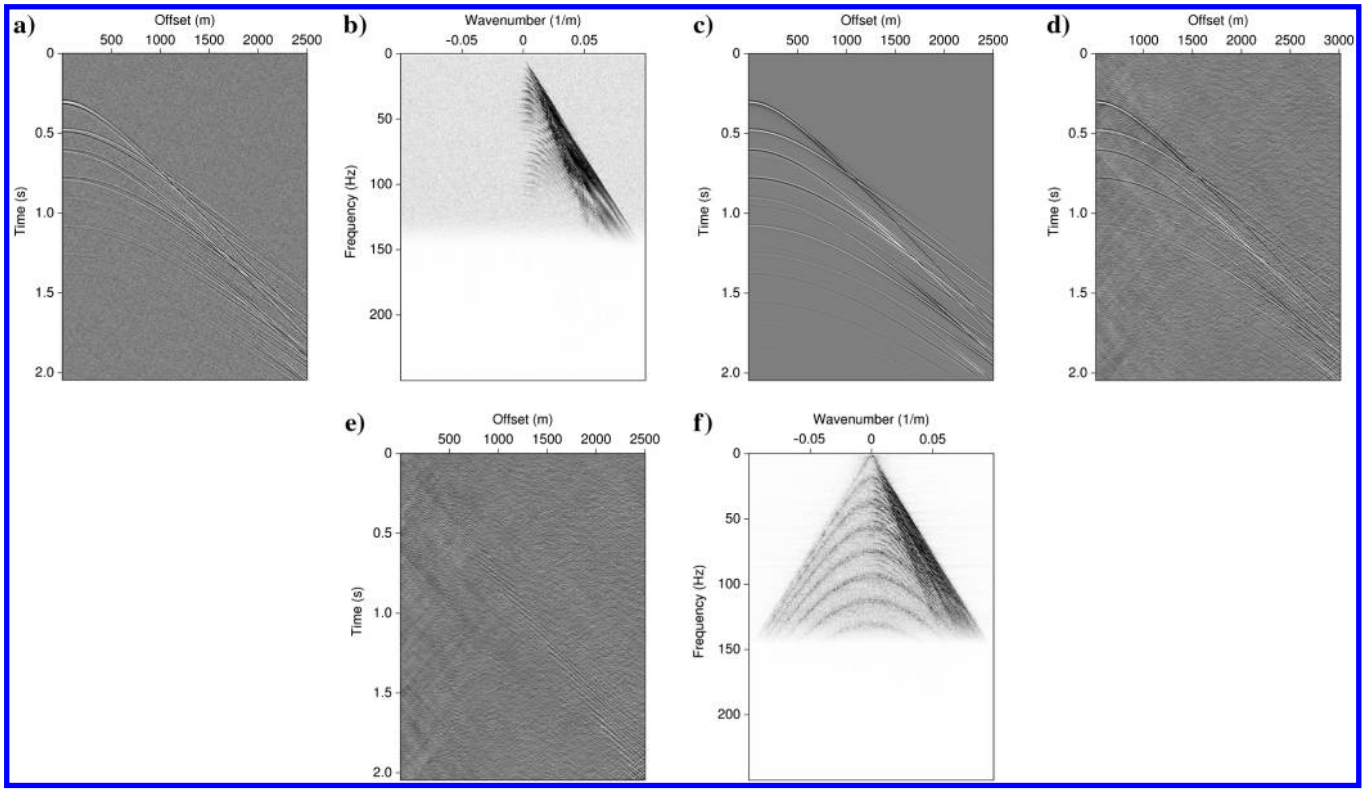

Figure 8. The modeled input scattered pressure wavefield shot gather for variable depth measurements (a), the f-k spectrum of the shot record (b), the modeled upgoing pressure wavefield at reference depth 7.5 m (c), the result of the conjugate gradient solution (d), the difference (e), and the f-k spectrum of the result obtained using the conjugate gradient solution (f).

depth is independent on the distance between source and receiver, located at a constant value of 25 m. Figure 7a shows the modeled input pressure wavefield shot gather. Figure 7b shows the f-k spectrum of the shot record. Note the notches in the section, showing frequency-wavenumber combinations in which no reflection energy is present. Figure 7c shows the modeled upgoing pressure wavefield at a reference receiver depth of 7.5 m. Figure 7d shows the results after using equation 64 derived in the previous section, and Figure 7e shows the difference between the computed results and the reference results. Note that the constant-depth streamer configuration is not able to cope with the spectral notches due to the singularities in the denominator of equation 64. As remarked, at the spectral notches, the scattered pressure wavefield contains no relevant data. Because the noise in the data has a random Gaussian distribution, the noise is severely enhanced for frequency-wavenumber combinations in which the spectral notches occur in the scattered input pressure data, which is demonstrated in Figure 7f. This occurs despite the complex frequencies that are used to avoid the singularities in the denominator of equation 64. It is remarked that the application of noise attenuation techniques prior to wavefield decomposition may reduce the impact of the spectral notches after wavefield decomposition. However, it must be realized that the results obtained become directly dependent on the geophysical integrity of the noise attenuation method(s) used.

Next, we will consider the same 2D example, but now only pressure measurements are available on the same variable-depth streamer used previously. Figure 8a shows the modeled input scattered pressure wavefield shot gather. Figure 8b shows the f-k spectrum of the shot record. Note that the notches in the section are less visible compared to the notches for the constant-depth streamer shown in Figure 7b, indicating that at these f-k combinations, now some reflection energy is present. The upgoing pressure wavefield can be obtained through equations 69 and 70, which, after discretization of the integral equation, can be obtained through a preconditioned conjugate gradient iterative scheme (van Borselen et al., 2009). Figure 8c shows the modeled upgoing pressure wavefield at a reference receiver depth of 7.5 m. Figure 8d shows the results after solving the discretized integral equation, and Figure 8e shows the difference between the computed results and the reference results. It is observed that the variable-depth streamer configuration is able to cope with the spectral notches reasonably well due to the "notch diversity" discussed in the previous section. However, some artifacts can still be seen. Figure 8f shows the f-k spectrum of the results obtained. It can be observed that noise has been blown up by the wavefield decomposition, in particular with a periodicity of around 18.75 Hz, which is caused by the notch related to the constant depth of 40 m of the streamer from offset 1500 m up to 2500 m.

CONCLUSIONS

In this paper, we have derived fundamental equations for wavefield decomposition for multisensor and single-sensor data, for depth-varying and depth-independent recordings from marine seismic experiments using a single- or dual-source configuration.

In marine seismic acquisition, source and receiver ghosts are generated when the energy generated by the seismic source, as well as any upgoing wavefield propagating upward from the subsurface, is reflected downward by the free surface. As a result, complex interference patterns between up- and downgoing wavefields are present in the recorded data, affecting the spectral bandwidth of the recorded data negatively. Wavefield decomposition is used to remove the ghost events present in the recorded data, thereby enhancing the spectral bandwidth and the resolution of the data.

A comparison is made between the results obtained for 2D synthetic example designed to highlight the strengths and weaknesses of the various acquisition configurations.

It is demonstrated that by using the proposed wavefield decomposition method, multisensor data (measurements of pressure and particle velocity components, or multidepth pressure measurements) allow for optimal wavefield decomposition as independent measurements are used to eliminate the interference patterns caused by the free surface. Single-sensor data using constant-depth recordings are shown to be incapable of producing satisfactory results in the presence of noise. Single-sensor data using a configuration with depth-varying measurements are able to deliver better results than when constant-depth recordings are used, but the results obtained are not of the same quality as when multisensor data are used.

ACKNOWLEDGMENTS

The authors thank R. Hegge, C. Riyanti, M. Frijlink, and W. Söllner for discussions. C. Riyanti is also thanked for her contributions to the numerical results presented. We also want to recognize the contributions of the late Svein Vaage to this work.

REFERENCES

Egan, M., K. G. El-Kasseh, and N. Moldoveanu, 2007, Full deghosting of OBC data with over/under source acquisition: 77th Annual International Meeting, SEG, Expanded Abstracts, 31–35.

Fokkema, J. T., and P. M. van den Berg, 1993, Seismic applications of acoustic reciprocity: Elsevier Science.

Moldoveanu, N., L. Combee, M. Egan, G. Hampson, L. Sydora, and W. Abriel, 2007, Over/under towed-streamer acquisition: A method to extend seismic bandwidth to both higher and lower frequencies: The Leading Edge, **26**, 41–58, doi: 10.1190/1.2431831.

Parkes, G., and S. Hegna, 2011, An acquisition system that extracts the earth response from seismic data: First Break, **29**, 81–87.

Pharez, S., N. Hendrick, and R. Tenghamn, 2008, First look at seismic data from a towed dual-sensor streamer: The Leading Edge, **27**, 904–907, doi: 10.1190/1.2954031.

Soubaras, R., and R. Dowle, 2010, Variable-depth streamer — A broadband marine solution: First Break, **28**, 89–96.

Tenghamn, R., and P. E. Dhelie, 2009, GeoStreamer — Increasing the signal-to-noise ratio using a dual-sensor towed streamer: First Break, **27**, 45–51.

van Borselen, R. G., J. T. Fokkema, and P. M. van den Berg, 2008, Method for deghosting marine seismic streamer data with irregular receiver positions: U.S. Patent Application 12/082,006.

van Borselen, R. G., J. T. Fokkema, and P. M. van den Berg, 2011, Methods and systems for deghosting marine seismic wavefields based on cost-functional minimization: U.S. Patent Application 13/407,049.